Nonlocal macroscopic models of multi-population pedestrian flows for walking facilities optimization

Paola Goatin, Daniel Inzunza, Luis Miguel Villada

Nonlocal macroscopic models of multi-population pedestrian flows for walking facilities optimization

Paola Goatin and Daniel Inzunza*
Luis Miguel Villada†

August 29, 2023

Abstract

We propose a nonlocal macroscopic pedestrian flow model for two populations with different destinations trying to avoid each other in a confined environment, where the nonlocal term accounts for anisotropic interactions, mimicking the effect of different cones of view, and the presence of walls or other obstacles in the domain. In particular, obstacles can be incorporated in the density variable, thus avoiding to include them in the vector field of preferred directions. In order to compute the solution, we propose a Finite Difference scheme that couples high-order WENO approximations for spatial discretization, a multi-step TVD method for temporal discretization, and a high-order numerical derivative formula to approximate the derivatives of nonlocal terms, and in this way avoid excessive calculations. Numerical tests confirm that each population manages to evade both the presence of the obstacles and the other population. The evacuation time problem is studied, in particular, the optimal position of the obstacles is obtained using a total travel time optimization processes.

Key words: nonlocal conservation laws; macroscopic pedestrian flow models; anisotropic interactions; WENO numerical schemes; domain shape optimization.

1 Introduction

We consider the class of nonlocal crowd dynamics models for two populations with different destinations trying to avoid each other in a confined environment and described by their densities ρ^1 and ρ^2. More precisely, we are interested in the following initial-boundary value problem for a non-local system of two conservation laws that describes the evolution of the pedestrian density $\boldsymbol{\rho} = (\rho^1, \rho^2)^T$ as a function of time t and position $\mathbf{x} = (x_1, x_2)$ on a walking domain $\Omega \subset \mathbb{R}^2$:

$$\begin{cases} \partial_t \boldsymbol{\rho} + \operatorname{div}_{\mathbf{x}} F\left(\boldsymbol{\rho}, \boldsymbol{\nu}\Big(\mathbf{x}, \mathcal{I}[\boldsymbol{\rho}(t)](\mathbf{x}), \hat{\mathcal{I}}[\nabla_{\mathbf{x}}\boldsymbol{\rho}(t)](\mathbf{x})\Big)\right) = 0, & \mathbf{x} \in \Omega, t \geq 0, \\ \boldsymbol{\rho}(0, \mathbf{x}) = \boldsymbol{\rho}_0(\mathbf{x}), & \mathbf{x} \in \Omega, \\ \boldsymbol{\rho}(t, \mathbf{x}) = 0, & \mathbf{x} \in \partial\Omega. \end{cases} \tag{1}$$

Here $\boldsymbol{\nu} = (\boldsymbol{\nu}^1, \boldsymbol{\nu}^2)^T$ with $\boldsymbol{\nu}^k = (\nu_1^k, \nu_2^k)$, $k = 1, 2$, are two vector fields that (with slight abuse of notation) are defined as

$$\boldsymbol{\nu}^k(t, \mathbf{x}) := \boldsymbol{\nu}^k\Big(\mathbf{x}, \mathcal{I}_k[\boldsymbol{\rho}(t)](\mathbf{x}), \hat{\mathcal{I}}_k[\nabla_{\mathbf{x}}\boldsymbol{\rho}(t)](\mathbf{x})\Big) = (1 - \epsilon_1 \mathcal{I}_k[\boldsymbol{\rho}(t)](\mathbf{x}))\boldsymbol{\mu}^k(\mathbf{x}) - \epsilon_2 \hat{\mathcal{I}}_k[\nabla_{\mathbf{x}}\boldsymbol{\rho}(t)](\mathbf{x}), \tag{2}$$

where $\boldsymbol{\mu}^k$ are the (normalized) fixed smooth vector fields of preferred directions (e.g., given by the regularized solution of an eikonal equation, which identifies the shortest path to destination), and

*Université Côte d'Azur, Inria, CNRS, LJAD. E-mail: {paola.goatin,daniel-eduardo.inzunza-herrera}@inria.fr
†GIMNAP-Departamento de Matemática, Universidad del Bío-Bío and CI^{2}MA-Universidad de Concepción-Concepción-Chile. E-mail: lvillada@ubiobio.cl

$\mathcal{I}_k[\boldsymbol{\rho}(t)]$, $\hat{\mathcal{I}}_k[\nabla_{\mathbf{x}}\boldsymbol{\rho}(t)]$ are non-local correction terms that depend on the current density distribution and its gradient, where the notation indicates a functional dependence, i.e., $\mathcal{I}_k$ (resp. $\hat{\mathcal{I}}_k$) depends on the function $\boldsymbol{\rho}(t) := \boldsymbol{\rho}(t,\cdot)$ (resp. $\nabla_{\mathbf{x}}\boldsymbol{\rho}(t) := \nabla_{\mathbf{x}}\boldsymbol{\rho}(t,\cdot)$) as a whole. Also, $\epsilon_1 > 0$ and $\epsilon_2 > 0$ are scaling factors, which temper the impact of the correction terms. In particular, we consider the following model introduced in [9]:

$$\begin{cases} \partial_t \rho^1 + \operatorname{div}_{\mathbf{x}}\left[\rho^1 v_1(\rho^1)\left(\left(1-\varepsilon_1\mathcal{I}_1[\rho^1+\rho^2]\right)\boldsymbol{\mu}^1(\mathbf{x}) - \varepsilon_2\hat{\mathcal{I}}_1[\nabla_{\mathbf{x}}\rho^2]\right)\right] = 0, \\ \partial_t \rho^2 + \operatorname{div}_{\mathbf{x}}\left[\rho^2 v_2(\rho^2)\left(\left(1-\varepsilon_1\mathcal{I}_2[\rho^1+\rho^2]\right)\boldsymbol{\mu}^2(\mathbf{x}) - \varepsilon_2\hat{\mathcal{I}}_2[\nabla_{\mathbf{x}}\rho^1]\right)\right] = 0, \end{cases} \tag{3}$$

where

$$\mathcal{I}_k[\rho] := \frac{\eta_k *_w \rho}{\sqrt{1+\|\eta_k *_w \rho\|^2}}, \qquad \hat{\mathcal{I}}_k[\nabla_{\mathbf{x}}\rho] := \frac{\eta_k *_w \nabla_{\mathbf{x}}\rho}{\sqrt{1+\|\eta_k *_w \nabla_{\mathbf{x}}\rho\|^2}} = \frac{\nabla_{\mathbf{x}}(\eta_k *_w \rho)}{\sqrt{1+\|\nabla_{\mathbf{x}}(\eta_k *_w \rho)\|^2}}.$$

Above, for $k = 1, 2$, η_k are smooth non-negative kernels with compact support such that $\iint_{\mathbb{R}^2} \eta_k(\mathbf{x})\,\mathrm{d}\mathbf{x} = 1$ and $v_k = v_k(\rho^k) > 0$ are the pedestrians' speed functions.
We remark hereby that the present framework can be easily generalized to more than two populations.

Aiming at reproducing the limited vision field of pedestrians, oriented towards the direction of movement, we follow the approach introduced in [3, 4, 9]. We consider conic convolution kernels constructed as follows: given a kernel function $\eta(\mathbf{x})$, we cut a conic section $\eta(\mathbf{x})\chi_{\mathcal{S}(\mathbf{x},l,\alpha,\boldsymbol{\gamma}_i)}(\mathbf{x})$ of angle 2α oriented in direction $\boldsymbol{\gamma}_k(\mathbf{x})$, $k = 1, 2$, which is described by the region

$$\mathcal{S}(\mathbf{x}, l, \alpha, \boldsymbol{\gamma}_i) = \left\{ \mathbf{y} \in \mathbb{R}^2 : \|\mathbf{y}-\mathbf{x}\| \le l, \frac{(\mathbf{y}-\mathbf{x})\cdot\boldsymbol{\gamma}_i(\mathbf{x})}{\|\mathbf{y}-\mathbf{x}\|\|\boldsymbol{\gamma}_i(\mathbf{x})\|} \ge \cos\alpha \right\}. \tag{4}$$

The section $\eta\chi_{\mathcal{S}(\mathbf{x},l,\alpha,\boldsymbol{\gamma}_i)}$ is smoothed by convolution with a Gaussian kernel $g(\mathbf{x}) = \exp(-(\|\mathbf{x}\|^2/2\sigma))$ with $\sigma = 5\times10^{-4}$, then normalized and finally shifted so that the maximum of the normalized smoothed kernel is centered in $(0,0)$, see Example 2 in [3] for more details.

The nonlocal terms, whose support can exceed the walking domain Ω, are problematic when dealing with boundaries, such as walls or other obstacles. In this work, we make the choice of incorporating the information in the convolution kernel, as originally proposed in [3, 7]. More precisely, we assume that $\Omega^c = \mathbb{R}^2 \setminus \Omega$ is a compact set consisting of a finite number $M \in \mathbb{N}$ of connected components $\Omega^c = \Omega_1^c \cup \ldots \cup \Omega_M^c$. As in [3] the convolution product $*_w$ is defined as

$$\Big(\eta *_w \rho(t)\Big)(\mathbf{x}) = \iint_{\mathbb{R}^2} \rho_w(t,\mathbf{y})\eta(\mathbf{x}-\mathbf{y})\,\mathrm{d}\mathbf{y}, \tag{5}$$

respectively

$$\Big(\eta *_w \nabla_{\mathbf{x}}\rho(t)\Big)(\mathbf{x}) = \iint_{\mathbb{R}^2} \rho_w(t,\mathbf{y})\nabla_{\mathbf{x}}\eta(\mathbf{x}-\mathbf{y})\,\mathrm{d}\mathbf{y},$$

where $\rho_w : \mathbb{R}^2 \to \mathbb{R}^+$ is the extension of the pedestrian density including the presence of obstacles:

$$\rho_w(t,\mathbf{x}) := \begin{cases} \rho(t,\mathbf{x}) & \text{if } \mathbf{x} \in \Omega, \\ R_{w_\ell} & \text{if } \mathbf{x} \in \Omega_\ell^c, \end{cases} \tag{6}$$

with $R_{w_\ell} \ge R > 0$, $\ell = 1, \ldots, M$, big enough so that $\boldsymbol{\nu}^k(t,\mathbf{x})\cdot\mathbf{n}(\mathbf{x}) \le 0$ for all $\mathbf{x} \in \partial\Omega$, $t \ge 0$, where $\mathbf{n}$ is the outward normal to Ω.

Remark 1 Note that, even in the worst case scenario $\boldsymbol{\mu}^k(\mathbf{x}) = \mathbf{n}(\mathbf{x})$ for some $\mathbf{x} \in \partial\Omega$, one can find R_{w_ℓ} big enough to guarantee $\boldsymbol{\nu}^k(t, \mathbf{x}) \cdot \mathbf{n}(\mathbf{x}) \leq 0$, provided that $1 < \varepsilon_1 + \varepsilon_2$. In particular, we can avoid including (some) obstacles in the preferred vector field $\boldsymbol{\mu} = (\boldsymbol{\mu}^1, \boldsymbol{\mu}^2)^T$, letting the nonlocal correction to account for their presence. This has the advantage to avoid the need of remeshing the computational domain and recomputing $\boldsymbol{\mu}$ if the obstacle positions are changes. Compared to other approaches [5, 6], which in this case would require the artificial construction of a "discomfort" vector field pointing inward the walking domain at its boundary to guarantee zero flux conditions, our choice greatly simplifies the numerical resolution of shape optimization problems, which can be addressed as classical PDE constrained optimization on a fixed computational domain.

In this work, we are interested in finding the optimal position of obstacles in front of exits to improve the pedestrian flow and minimize the evacuation time in walking facilities. In the last two decades, this problem has made the object of several investigations employing different techniques [6, 8, 11, 13, 15, 17], and we believe that our approach offers new perspectives to efficiently handle the problem. Nevertheless, the computational cost related to the presence of nonlocal terms poses severe limitations to the implementation of optimization routines. For this reason, we also propose an optimized version of the high order Runge-Kutta WENO finite difference scheme developed in [3], which minimizes the number of (discretized) convolution products to be computed, thus greatly improving the simulation time.

The rest of the paper is organized as follows. Section 2 recalls the regularity hypotheses and resumes the analytical properties of (1), its numerical discretization is described in Section 3 and the shape optimization problem is formulated in Section 4. Finally, Section 5 collects the corresponding numerical tests.

2 Model analysis

Well-posedness of general system of nonlocal conservation laws couple in the integral terms was first studied in [1]. Below, we summarize the necessary assumptions concerning the domain Ω and the functions v_k, $\boldsymbol{\nu}^k$, $\boldsymbol{\mu}^k$ and η_k, $k = 1, 2$:

(I1) The domain $\Omega \subset \mathbb{R}^2$ is a non-empty bounded open set with smooth boundary $\partial\Omega$, so that the outward normal $\mathbf{n}(\mathbf{x})$ is uniquely defined for all $\mathbf{x} \in \partial\Omega$.

(I2) The vector fields $\boldsymbol{\nu}^k$ point inward along the boundary $\partial\Omega$ of Ω, i.e., $\boldsymbol{\nu}^k(t, \mathbf{x}) \cdot \mathbf{n}(\mathbf{x}) \leq 0$ for all $\mathbf{x} \in \partial\Omega$, $t \geq 0$.

(I3) The speed functions $v_k \in \mathbf{C^2}(\mathbb{R}; \mathbb{R}_+)$ are non-increasing, $v_k(0) = V^k_{\max}$ and $v_k(R) = 0$ for some constants $V^k_{\max}, R > 0$.

(I4) The vector fields of preferred directions $\boldsymbol{\mu}^k \in (\mathbf{C^2} \cap \mathbf{W^{2,\infty}})(\mathbb{R}^2; \mathbb{R}^2)$ are defined such that $\operatorname{div} \boldsymbol{\mu}^k \in (\mathbf{W^{1,1}} \cap \mathbf{W^{1,\infty}})(\mathbb{R}^2; \mathbb{R})$.

(I5) The kernel functions $\eta_k \in (\mathbf{C^3_c} \cap \mathbf{W^{3,\infty}})(\mathbb{R}^2; \mathbb{R}^+)$ satisfy $\iint_{\mathbb{R}^2} \eta_k(\mathbf{x})\, \mathrm{d}\mathbf{x} = 1$.

Assumption **(I2)** guarantees the invariance of the domain Ω, i.e. if $\operatorname{supp} \rho^k(0, \cdot) \subset \Omega$, then we have that $\operatorname{supp} \rho^k(t, \cdot) \subset \Omega$ for all $t > 0$, so that the boundary condition become useless and the problem can be studied on the whole plane $\mathbb{R}^2$. Solutions of problem (1) are then intended in the following sense.

Definition 1 [2, Def. 2.1] *For any $T > 0$ and $\boldsymbol{\rho}_0 \in \mathbf{L^1}(\mathbb{R}^2, [0,R]^2)$ such that* $\operatorname{supp} \boldsymbol{\rho}_0 \subset \Omega$*, a function $\boldsymbol{\rho} \in \mathbf{C^0}([0,T], \mathbf{L^1}(\mathbb{R}^2; [0,R]^2)$ is said to be a* weak entropy solution *to* (1) *if, for $k = 1, 2$, ρ^k is a Kružkov entropy solution to the Cauchy problem*

$$\begin{cases} \partial_t \rho^k + \operatorname{div}_{\mathbf{x}} F^k\left(\rho^k, \nu^k(t,\mathbf{x})\right) = 0, & \mathbf{x} \in \Omega, t \geq 0, \\ \rho^k(0,\mathbf{x}) = \rho_0^k(\mathbf{x}), & \mathbf{x} \in \Omega, \end{cases} \tag{7}$$

i.e., for all $\kappa \in \mathbb{R}$ and all test functions $\phi \in \mathbf{C_c^\infty}(]-\infty, T[\times \mathbb{R}^2; \mathbb{R}^+)$ there holds

$$\begin{aligned} &\int_0^T \int_{\mathbb{R}^2} \left\{ \left|\rho^k - \kappa\right| \partial_t \phi + \operatorname{sgn}(\rho^k - \kappa)\Big(F^k\left(\rho^k, \nu^k(t,\mathbf{x})\right) - F^k\left(\kappa, \nu^k(t,\mathbf{x})\right)\Big) \cdot \nabla_{\mathbf{x}} \phi \right\} \mathrm{d}\mathbf{x}\, \mathrm{d}t \\ &- \int_0^T \int_{\mathbb{R}^2} \operatorname{div}_{\mathbf{x}} F^k\left(\kappa, \nu^k(t,\mathbf{x})\right) \operatorname{sgn}(\rho^k - \kappa) \phi \, \mathrm{d}\mathbf{x}\, \mathrm{d}t + \int_{\mathbb{R}^2} \left|\rho_0^k(\mathbf{x}) - \kappa\right| \phi(0,\mathbf{x})\, \mathrm{d}\mathbf{x} \geq 0. \end{aligned} \tag{8}$$

The existence of solutions follows from [1, 2], see [2, Section 3] in particular for an application to a system similar to (3). Indeed, (3) fits [2, Eq. (1.1)] and thus [2, Lemma 3.1] setting $N = 2$, $m = 6$ and

$$\eta = \theta = \begin{bmatrix} \eta_1 & \partial_{x_1}\eta_2 & \partial_{x_2}\eta_2 & \eta_2 & 0 & 0 \\ \eta_1 & 0 & 0 & \eta_2 & \partial_{x_1}\eta_1 & \partial_{x_2}\eta_1 \end{bmatrix}.$$

Therefore, [2, Theorem 2.2] holds under the above assumptions:

Theorem 1 *Let assumptions* **(I1)**-**(I5)** *hold. For any initial datum $\boldsymbol{\rho}_0 \in \left(\mathbf{L^1} \cap \mathbf{L^\infty} \cap BV\right)(\Omega; [0,R]^2)$, there exists a solution $\boldsymbol{\rho} \in \mathbf{C^0}(\mathbb{R}_+, \mathbf{L^1}(\Omega; [0,R]^2))$ of* (1), (3) *in the sense of Definition 1. Moreover, the following bounds hold*

$$\begin{aligned} &\left\|\boldsymbol{\rho}(t,\cdot)\right\|_{\mathbf{L^1}(\Omega;[0,R]^2)} = \left\|\boldsymbol{\rho}_0\right\|_{\mathbf{L^1}(\Omega;[0,R]^2)}, \\ &TV(\boldsymbol{\rho}(t,\cdot)) \leq e^{\mathcal{K}_1 t} TV(\boldsymbol{\rho}_0) + \mathcal{K}_2(e^{\mathcal{K}_1 t} - 1), \\ &\left\|\boldsymbol{\rho}(t+\tau,\cdot) - \boldsymbol{\rho}(t,\cdot)\right\|_{\mathbf{L^1}(\Omega;[0,R]^2)} \leq C(t)\tau, \end{aligned}$$

where $\mathcal{K}_1$, $\mathcal{K}_2$ and $C(t)$ are constant depending on $\|\boldsymbol{\rho}_0\|_{\mathbf{L^1}}$, $TV(\boldsymbol{\rho}_0)$ and on v_k, μ^k, η_k for $k = 1, 2$.

Remark 2 By the specific choice of the flux function F made in (3) and assumption **(I3)**, we have that $F^k\left(0, \nu^k(t,\mathbf{x})\right) = F^k\left(R, \nu^k(t,\mathbf{x})\right) = 0$. Therefore, a trivial application of the comparison principle implies that the maximum principle holds, i.e., if $\rho_0^k(\mathbf{x}) \in [0,R]$ for all $\mathbf{x} \in \Omega$, then $\rho^k(t,\mathbf{x}) \in [0,R]$ for all $\mathbf{x} \in \Omega$ and $t > 0$, $k = 1, 2$.

3 High-resolution numerical scheme

3.1 Notation and semi-discrete formulation

We consider a rectangular computational domain $D =]a,b[\times]c,d[$ and we use a Cartesian grid with nodes (x_1^i, x_2^j), $i = 1, \ldots, N_1$, and $j = 1, \ldots, N_2$, such that $x_1^i = (i - 1/2)h_1$, $x_2^j = (j - 1/2)h_2$, where $h_1 = (b-a)/N_1$ and $h_2 = (d-c)/N_2$. This provides $N_1 \times N_2$ grid points $\mathbf{x_i} := (x_1^i, x_2^j)$, where $\mathbf{i} = (i,j) \in \mathcal{M} := \{1, \ldots, N_1\} \times \{1, \ldots, N_2\}$. Moreover, the two dimensional unit vectors $\mathbf{e}_1 := (1,0)$ and $\mathbf{e}_2 := (0,1)$ allow to denote neighbouring grid points as $\mathbf{x_{i+e_1}} = (x_1^{i+1}, x_2^j)$ and

$\mathbf{x}_{\mathbf{i}+\mathbf{e}_2} = (x_1^i, x_2^{j+1})$. As in [3, 9], we denote by $\boldsymbol{u} : [0, +\infty[\to \mathbb{R}^{2\times N_1\times N_2}$ the solution of (1) computed at time t in the grid points where

$$u_{k,\mathbf{i}}(t) = \rho^k(t, \mathbf{x}_\mathbf{i}), \quad \mathbf{F}_{k,\mathbf{i}} = F^k\left(\rho^k(t, \mathbf{x}_\mathbf{i}), \nu^k(t, \mathbf{x}_\mathbf{i})\right) \qquad \text{for } k = 1, 2 \text{ and } \mathbf{i} \in \mathcal{M}.$$

In order to define a numerical scheme, first we approximate the solution of (1) in a semi-discrete form by a system of ODEs

$$\frac{\mathrm{d}\boldsymbol{u}}{\mathrm{d}t} = \mathcal{C}(\boldsymbol{u}), \tag{9}$$

where $\mathcal{C}(\boldsymbol{u})$ is the spatial discretization of the convective term with entries given by

$$\mathcal{C}(\boldsymbol{u}) = \big(\mathcal{C}(\boldsymbol{u})_\mathbf{i}\big)_{\mathbf{i}\in\mathcal{M}} \quad \text{with} \quad \mathcal{C}(\boldsymbol{u})_{k,\mathbf{i}} = -\sum_{l=1}^{2} \frac{1}{h_l}\left(\hat{f}_{k,\mathbf{i}+\frac{1}{2}\mathbf{e}_l} - \hat{f}_{k,\mathbf{i}-\frac{1}{2}\mathbf{e}_l}\right),$$

for suitable numerical fluxes $\hat{f}_{k,\mathbf{i}+\frac{1}{2}\mathbf{e}_l}$ for $k, l = 1, 2$ obtained by WENO reconstructions of split fluxes. For the numerical flux $f_k = \hat{f}_{k,\mathbf{i}+\frac{1}{2}\mathbf{e}_l}$, the Lax-Friedrichs-type flux splitting $f_k^\pm(\rho)$ is given by

$$f_k^\pm(\rho) = \frac{1}{2}\left(f_k(\rho) \pm \alpha_k\rho\right), \qquad \alpha_k = \max_{l=1,2}\max_{\rho^k}\left|\partial_{\rho^k}(\rho^k v_k(\rho^k))\right| \sup_{\mathbf{x}\in\Omega} |\,\nu(\mathbf{x})\cdot\mathbf{e}_l|.$$

If $\mathcal{R}^\pm\left(f_{k,\mathbf{i}+(-r:r)\mathbf{e}_l}\right) = \mathcal{R}^\pm\left(f_{k,\mathbf{i}-r\mathbf{e}_l}, \ldots, f_{k,\mathbf{i}+r\mathbf{e}_l}\right)$ denotes $(2r-1)$th-order WENO upwind-biased reconstructions for $r = 2, 3, 4$, then

$$\hat{f}_{k,\mathbf{i}+\frac{1}{2}\mathbf{e}_l} = \mathcal{R}^+\left(f^+_{k,\mathbf{i}+(-r:r)\mathbf{e}_l}\right) + \mathcal{R}^-\left(f^-_{k,\mathbf{i}+(-r+1:r+1)\mathbf{e}_l}\right), \qquad k, l = 1, 2,$$

see [14, 16]. In this work we consider third-order of accuracy in space with $r = 2$.

3.2 Discretization of the convolution term

In order to evaluate the non-local terms in (3), where the convolution term $*_w$ is defined by (5), the corresponding convolutions $(\eta_1 *_w \rho^1), (\eta_1 *_w \rho^2), (\partial\eta_1/\partial x_1 *_w \rho^2), (\partial\eta_1/\partial x_2 *_w \rho^2)$ and $(\eta_2 *_w \rho^1), (\eta_2 *_w \rho^2), (\partial\eta_2/\partial x_1 *_w \rho^1), (\partial\eta_2/\partial x_2 *_w \rho^1)$ are calculated approximately on the discrete grid via a quadrature formula, in our cases a composite Simpson rule. Since $\mathrm{supp}(\eta) \subset [-n_0h, n_0h] \times [-n_0h, n_0h]$ for $n_0 \in \mathbb{N}$ large enough, any convolution product is given by

$$\Big(\eta * \rho(t)\Big)(\mathbf{x}_\mathbf{i}) \approx \sum_{p=-n_0}^{n_0}\sum_{q=-n_0}^{n_0} h^2 c_p c_q \rho(t, \mathbf{x}_{\mathbf{i}-\mathbf{p}})\eta(\mathbf{x}_\mathbf{p}),$$

where c_p and c_q are the coefficients in the quadrature rule and $\mathbf{p} = (p, q)$. For $\mathbf{u} = (u_\mathbf{i}) \in \mathbb{R}^{M\times N}$ and for the convolution product (5), this formula can be written as

$$(\eta *_w u)(\mathbf{x}_\mathbf{i}) = \sum_{p=-n_0}^{n_0}\sum_{q=-n_0}^{n_0} h^2 c_p c_q u_{w,\mathbf{i}-\mathbf{p}}\eta(\mathbf{x}_\mathbf{p}), \tag{10}$$

where $u_{w,\mathbf{i}}$ is a discrete version of the function (6) defined by

$$u_{w,\mathbf{i}} = \begin{cases} u_{\mathbf{i}} & \text{if } \mathbf{x_i} \in \Omega \setminus \Omega^c, \\ R_{w_\ell} & \text{if } \mathbf{x_i} \in \Omega^c_\ell, \\ 0 & \text{if } \mathbf{x_i} \in \Omega_E, \end{cases} \tag{11}$$

where Ω^c_ℓ corresponds to the component representing walls and obstacles and $\Omega_E \subset \Omega^c$ is such that $\overline{\Omega}_E \cap \overline{\Omega} := \Gamma_E$ corresponds to the exits, where we apply absorbing boundary conditions.
Clearly, the discrete convolution (10) causes a computational bottleneck. This is a classical problem in scientific computing that is effectively handled by fast convolution algorithms, mainly based on Fast Fourier Transforms [18].

Finally, the semi-discrete scheme (9) is discretized by a third-order TVD Runge-Kutta time discretization method

$$\begin{aligned} \boldsymbol{u}^{(1)} &= \boldsymbol{u}^n + \Delta t\, \mathcal{C}(\boldsymbol{u}^n)\,, \\ \boldsymbol{u}^{(2)} &= \tfrac{3}{4}\boldsymbol{u}^n + \tfrac{1}{4}\left(\boldsymbol{u}^{(1)} + \Delta t\, \mathcal{C}(\boldsymbol{u}^{(1)})\right), \\ \boldsymbol{u}^{n+1} &= \tfrac{1}{3}\boldsymbol{u}^n + \tfrac{2}{3}\left(\boldsymbol{u}^{(2)} + \Delta t\, \mathcal{C}(\boldsymbol{u}^{(2)})\right). \end{aligned} \tag{12}$$

The numerical solution of the system of ODEs (9) using the integration (12) is called FD-RK-WENOk, where k is the order of the WENO approach used.

3.3 A fast, high-order multi-step scheme

In order to reduce the computational cost and improve the performance of the above algorithm, we proceed as follow: to evaluate the non-local terms, first the convolution term $(\eta_1 *_w \rho^1), (\eta_1 *_w \rho^2)$ and $(\eta_2 *_w \rho^1), (\eta_2 *_w \rho^2)$ are computed approximately on the discrete grid via the quadrature formula (10), then the terms $(\partial\eta_1/\partial x_1 *_w \rho^2), (\partial\eta_1/\partial x_2 *_w \rho^2)$ and $(\partial\eta_2/\partial x_1 *_w \rho^1), (\partial\eta_2/\partial x_2 *_w \rho^1)$ are approximated using a fourth-order centered difference approximation of the first

$$((\partial\eta/\partial x_l) *_w \rho)(\mathbf{x_i}) = \frac{-(\eta *_w u)(\mathbf{x_{i+2e}}_l) + 8(\eta *_w u)(\mathbf{x_{i+e}}_l) - 8(\eta *_w u)(\mathbf{x_{i-e}}_l) + (\eta *_w u)(\mathbf{x_{i-2e}}_l)}{12h_l}, \tag{13}$$

for $l = 1, 2$.

Finally, the semi-discrete scheme (9) is discretized by a multi-step method with the TVD property [10]

$$\boldsymbol{u}^{n+1} = \frac{16}{27}\left(\boldsymbol{u}^n + 3\Delta t\, \mathcal{C}(\boldsymbol{u}^n)\right) + \frac{11}{27}\left(\boldsymbol{u}^{n-3} + \frac{12}{11}\Delta t\, \mathcal{C}(\boldsymbol{u}^{n-3})\right). \tag{14}$$

We use the FD-RK-WENOk scheme to compute the first three approximations $\boldsymbol{u}^1, \boldsymbol{u}^2$ and $\boldsymbol{u}^3$. The numerical solution of system of ODEs (9) using the formulas (13) and the integration (14) is called FD-MS-WENOk, where k is the order of the WENO approach used.
Observe that, to obtain an approximation from t^n to $t^n + \Delta t$, while the FD-RK-WENOk requires calculating 3×8 convolution terms, the FD-MS-WENOk scheme require only 1×4 convolution evaluations plus the computation of 4 numerical derivatives (13).

4 Optimization of obstacle positions for evacuation problems

Let us denote by $\Omega_{\text{opt}} := \cup_{\ell \in \mathcal{I}_{\text{opt}}} \Omega^c_\ell \subseteq \Omega^c$, with $\mathcal{I}_{\text{opt}} \subseteq \{1, \ldots, M\}$, the set of obstacles / walls whose positions we want to optimize to minimize the evacuation time. Since their impact is incorporate

in the dynamics through the extended convolution product (5)-(6) and not as zero-flux boundary conditions, neither in the fixed vector field $\boldsymbol{\mu}$, the underlying domain shape optimization problem reduces to a simpler PDE-constrained optimization, which in particular does not require adaptive meshes.

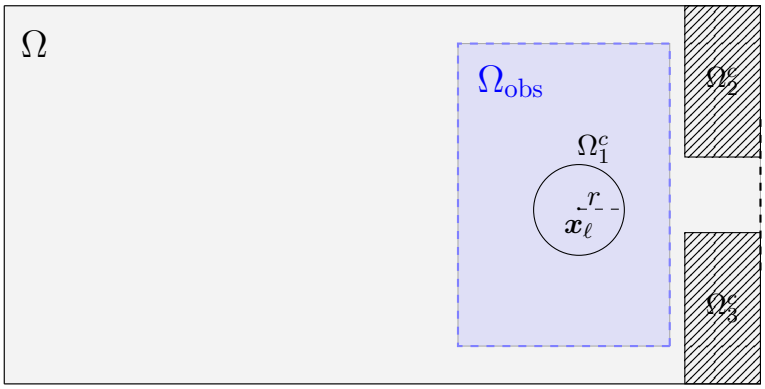

Figure 1: Example of walking domain Ω and set of obstacles/walls with $\Omega_{\text{opt}} = \Omega_1^c$.

The optimization problem considered in this work consists of minimizing the total travel time of pedestrians, depending on the obstacle positions. Let $\mathbf{x}_\ell \in \Omega_\ell^c$, $\ell \in \mathcal{I}_{\text{opt}}$, be a reference coordinate for each control obstacle. The optimization problem consists then in finding

$$T_{\text{opt}} := \min_{\substack{\mathbf{x}_\ell \in \Omega_{\text{obs}} \\ \ell \in \mathcal{I}_{\text{opt}}}} \mathrm{T}(\ell) = \min_{\substack{\mathbf{x}_\ell \in \Omega_{\text{obs}} \\ \ell \in \mathcal{I}_{\text{opt}}}} \int_{\mathbb{R}^+} \int_\Omega \boldsymbol{\rho}(t, \mathbf{x}) \, \mathrm{d}\mathbf{x} \, \mathrm{d}t \,, \tag{15}$$

where $\Omega_{\text{obs}} \subseteq \mathbb{R}^2$ is a predefined subset of admissible obstacle positions and $\boldsymbol{\rho}$ is the solution of (3) on the domain Ω, which depend on the obstacle positions $\mathbf{x}_\ell$, $\ell \in \mathcal{I}_{\text{opt}}$, see Figure 1.

The above PDE-constrained optimization problem is generally non convex, and can be solved numerically by standard algorithms involving gradient descent or stochastic optimization. To avoid local minima, we made the choice to solve problem (15) using the MATLAB Bayesian optimizer `bayesopt`, which operates a Gaussian process model to minimize the objective function, thus better exploring the admissible control domain.

We aim to optimize the total travel time of the evacuation domain by finding the coordinates $\mathbf{x}_\ell$, $\ell \in \mathcal{I}_{\text{opt}}$, of the balls with fixed radius r_ℓ, $\mathbf{B}(\mathbf{x}_\ell, r_\ell) \subset \Omega_{\text{obs}}$. We initialize each $\mathbf{x}_\ell$ by choosing it arbitrarily in Ω_{obs}. The prescribed maximal iteration number is $10 \times 2 \times \left|\mathcal{I}_{\text{opt}}\right|$, where $\left|\mathcal{I}_{\text{opt}}\right|$ is the cardinality of $\mathcal{I}_{\text{opt}}$, and for each optimization we output the optimal cost value, and the computation time T_{comp}.

5 Numerical tests

In this Section, we aim at investigating the effects of the non-local operator (5)-(6) from the crowd dynamics modelling point of view, and also we check the effectiveness of the high-resolution numerical scheme proposed in Section 3.3. To this end, we approach numerically the solution $\boldsymbol{\rho}(t, \mathbf{x})$ of (3)-(6) for $(t, \mathbf{x}) \in [0, T] \times \Omega$ by using the multi-step scheme (14) with a third-order WENO reconstruction labeled FD-MS-WENO3, obtaining a vector solution $\boldsymbol{u}^n$ at the $N_1 \times N_2$ grid points $\mathbf{x}_\mathbf{i} := (x_1^i, x_2^j)$, where $\mathbf{i} = (i, j) \in \mathcal{M} := \{1, \dots, N_1\} \times \{1, \dots, N_2\}$, such that $u_{k,\mathbf{i}}^n \approx \rho^k(t^n, \mathbf{x}_\mathbf{i})$ for $k = 1, 2$ and $n = 0, 1, 2, \dots$.

In all the examples below, we consider the speed functions and the kernel functions [6] given by

$$v_k(\rho) = V_k^{\max}(1-\rho), \quad \eta_k(\mathbf{x}) = \eta(\mathbf{x}) = \frac{315}{128\pi l^{18}}(l^4 - \|\mathbf{x}\|^4)^4 \chi_{[0,l]}(\|\mathbf{x}\|),$$

and a conic section $\eta(\mathbf{x})\chi_{\mathcal{S}(\mathbf{x},l,\alpha,\boldsymbol{\gamma}_i)}(\mathbf{x})$ of angle 2α oriented in direction $\boldsymbol{\gamma}_k(\mathbf{x})$ for $k = 1, 2$, where $\mathcal{S}(\cdot)$ is given by (4) and the other parameters are specified in each example.

For each iteration, the time step Δt in (14) is determined by the formula

$$\frac{\Delta t}{h}\max\{\alpha_1, \alpha_2\} = \frac{1}{3}C_{\text{cfl}},$$

where C_{cfl} as the largest multiple of 0.05 that yields oscillation-free numerical solutions. In all numerical tests we have used $C_{\text{cfl}} = 0.2$.

5.1 Example 1: Comparing FD-MS-WENO3 and FD-RK-WENO3 numerical schemes

In this example, we consider a single population model and compare the FD-MS-WENO3 scheme proposed in Section 3.3 with the the FD-RK-WENO3 scheme used in [3]. We consider $\Omega = [0, 3]^2$ a corridor with exit door at $\Gamma_E = \{3\} \times [0, 3]$. In order to include the presence of the lateral walls in the nonlocal term (10), we put in the extended function $u_{w,\mathbf{i}}$ in (11), $R_{\omega_1} = 1$. The vector field and the others model parameters are given by

$$V^{\max} = 4, \quad \boldsymbol{\nu}(t, \mathbf{x}) = (1, 0) - 0.6\hat{\mathcal{I}}[\nabla_{\mathbf{x}}\rho(t)](\mathbf{x}), \quad l = 0.6, \quad \boldsymbol{\gamma}(\mathbf{x}) = (1, 0), \quad \alpha = \pi.$$

Initial condition is given by $\rho_0(\mathbf{x}) = e^{-10\|\mathbf{x}-(1,1.5)\|^2}$, and the reference solution at $T = 0.5$ is computed using the FD-RK-WENO3 scheme with 1920^2 points. Table 1 shows the approximate $\mathbf{L^1}$-error, the experimental order accuracy and the CPU-times for both schemes. We infer that FD-MS-WENO3 scheme is always more efficient than the FD-RK-WENO3 scheme, with speedup factors above 9, which is evident given that, in the multi-step scheme, only the calculation of a non-local term is required when advancing one temporal step.

$T = 0.5$	MS-WENO3			RK-WENO3		
$N_1 \times N_2$	L^1-error	e.o.a.	cpu-time	error	e.o.a.	cpu-time
30×30	1.3e-3	–	6.0e-2	1.2e-3	–	4.2e-1
60×60	3.0e-4	2.1	1.2e-1	2.7e-4	2.1	1.2e0
120×120	5.7e-5	2.4	1.2e+0	5.6e-5	2.2	1.1e2
240×240	9.4e-6	2.6	1.2e+1	1.0e-5	2.4	9.1e2
480×480	1.4e-3	2.9	1.1e+2	1.6e-6	2.6	9.3e3

Table 1: Example 1: Comparing the efficiency of FD-MS-WENO3 and FD-RK-WENO3 numerical schemes.

5.2 Example 2: Bidirectional flow in a corridor with obstacles

In this example, we consider a pedestrian flow with two populations traveling in a corridor in opposite directions, including the presence of three obstacles in the corridor. The exit doors of each population are located at $\Gamma_{E,1} = \{4\} \times [0, 2]$ and $\Gamma_{E,2} = \{0\} \times [0, 2]$ for ρ^1 and ρ^2 respectively. This problem can be modeled by equations (3) in $\Omega = [0, 4] \times [0, 2] - (\Omega_1^c \cup \Omega_2^c \cup \Omega_3^c)$, where

$$\Omega_1^c = \mathbf{B}((1.5, 0.5), 0.1), \quad \Omega_2^c = \mathbf{B}((1.5, 1.5), 0.1), \quad \Omega_3^c = \mathbf{B}((2.5, 1), 0.2),$$

which represent the position of the obstacles, where $\mathbf{B}(\mathbf{x}_0, r)$ denotes the ball centered in $\mathbf{x}_0$ and radius r. The vector fields are fixed and oriented towards the respective exits, i.e. $\boldsymbol{\mu}^1(\mathbf{x}) = (1, 0)$ and $\boldsymbol{\mu}^2(\mathbf{x}) = (-1, 0)$ respectively, and the other parameters are given by

$$V_1^{\max} = 4, \quad \boldsymbol{\gamma}^1(\mathbf{x}) = (1, 0) \quad l = 0.3, \quad \alpha_1 = \frac{\pi}{3}, \quad \varepsilon_1 = 0.6,$$
$$V_2^{\max} = 4, \quad \boldsymbol{\gamma}^2(\mathbf{x}) = (-1, 0) \quad l = 0.5, \quad \alpha_2 = \frac{\pi}{3}, \quad \varepsilon_2 = 0.8.$$

The initial conditions and the vector fields are display in Figure 2 with

$$\begin{bmatrix} \rho_0^1 \\ \rho_0^2 \end{bmatrix}(\mathbf{x}) = \begin{bmatrix} 0.9\chi_{]0.4,1.1[\times]0.6,1.4[} \\ 0.85\chi_{]3,3.5[\times]0.4,0.6[} \end{bmatrix}(\mathbf{x}), \quad \mathbf{x} \in \Omega\,.$$

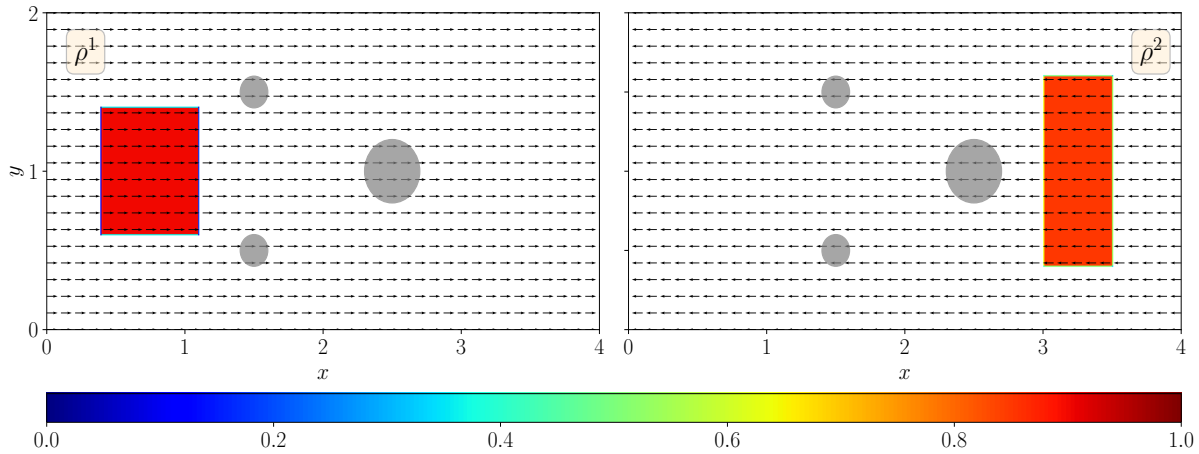

Figure 2: Example 2: Initial condition ρ_0^k and vector field $\boldsymbol{\mu}^k$ for each species $k = 1, 2$.

In order to include the presence of the obstacles in the computational domain, we put $R_{\omega_1} = R_{\omega_2} = R_{\omega_3} = 1.1$ in the evaluation the nonlocal terms. In Figure 3 we display numerical solution for ρ^1 and ρ^2 at simulation times $T = 0.5,\ 3.0,\ 7.0$ computed with FD-MS-WENO3 scheme with 320×640 points ($h = 1/160$). We observe that each group manages to evade the presence of the obstacles. At the same time, both populations scale their speed according to the total density and deviate from their preferred trajectory if the other group is in their view horizon.

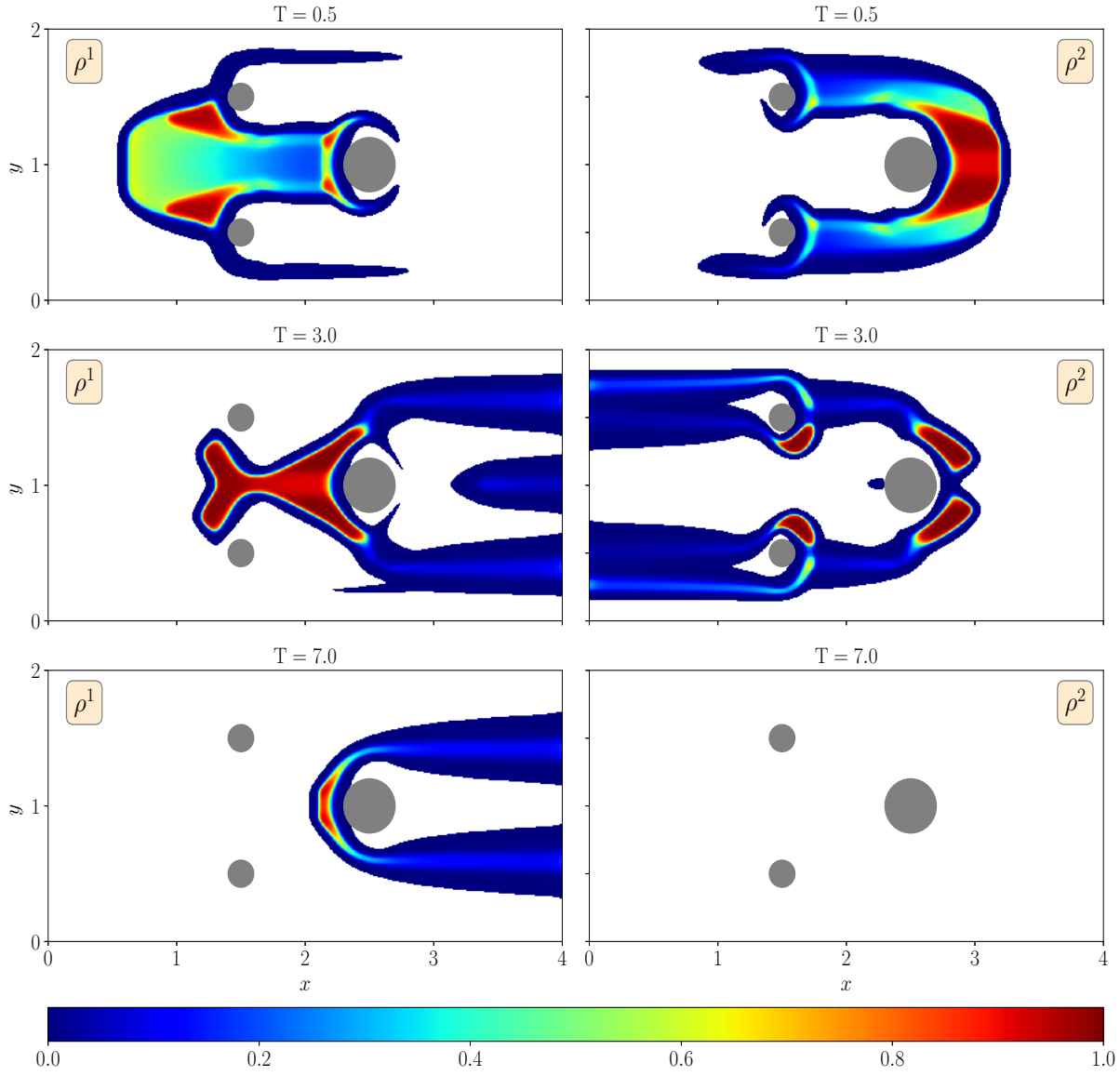

Figure 3: Example 2: Evacuation dynamics with obstacle, for angle 2α with $\alpha = \pi/3$, at simulated times $T = 0.5,\ 3,\ 7$, for densities ρ^1 (left column) and ρ^2 (right column) respectively.

5.3 Example 3: Optimization of obstacle position in a cross domain

In this example, we consider the problem of evacuating two populations ρ^1 and ρ^2 from a domain consisting of two perpendicularly intersecting corridors. We are interested in studying the impact of an obstacle located at the corridor crossing area and how its strategic position can improve the total travel time in the evacuation dynamic. The obstacle consists of a column of cross section $\mathbf{B}(\mathbf{x}_0, r)$, a ball centered in $\mathbf{x}_0 \in \Omega_{\text{obs}}$ and radius r. The space available to the populations is the cross section

$$\Omega =]-3,3[\times]-0.5,0.5[\cup]-0.5,0.5[\times]-3,3[\setminus \Omega_1^c\,,$$

where the exit doors are located at $\Gamma_1 = \{3\}\times]-0.5,0.5[$ and $\Gamma_2 =]-0.5,0.5[\times\{3\}$ and

$$\Omega_1^c = \mathbf{B}(\mathbf{x}_0, 0.125), \quad \Omega_{\text{obs}} =]-0.5,0.5[\times]-0.5,0.5[\,, \quad \mathcal{I}_{\text{opt}} = \{1\},$$

see Figure 4.

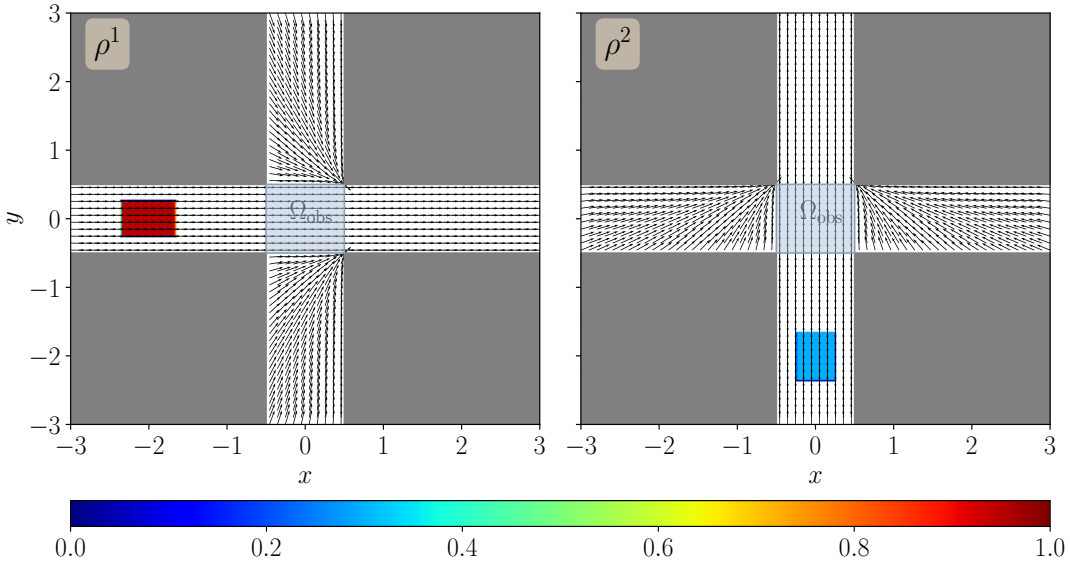

Figure 4: Example 3: Initial condition ρ_0^k and vector field $\boldsymbol{\mu}^k$ for each species $k = 1, 2$.

The vectors fields, $\boldsymbol{\mu}^1(\mathbf{x})$ and $\boldsymbol{\mu}^2(\mathbf{x})$ are computed setting $\boldsymbol{\mu}^i(\mathbf{x}) = -\nabla\phi_i(\mathbf{x})$ for $i = 1, 2$, where ϕ_i are the solutions of the Eikonal equations

$$\begin{cases} |\nabla\phi_i(\mathbf{x})| = 1, & \mathbf{x} \in \hat{\Omega} :=]-3,3[\times]-0.5,0.5[\cup]-0.5,0.5[\times]-3,3[\,, \\ \phi_i(\mathbf{x}) = 1 & \mathbf{x} \in \partial\hat{\Omega}\setminus\Gamma_i\,, \\ \phi_i(\mathbf{x}) = 0, & \mathbf{x} \in \Gamma_i\,. \end{cases} \qquad i = 1, 2$$

It is important to note that we have not consider the presence of the obstacle Ω_1^c when computing the solutions of the Eikonal equations.

The initial condition is displayed in Figure 4. The orientation of the vision field and and other parameters are given by

$$\begin{bmatrix} \rho_0^1 \\ \rho_0^2 \end{bmatrix}(\mathbf{x}) = \begin{bmatrix} 0.95\chi_{]-2.35,-1.65[\times]-0.25,0.25[} \\ 0.3\chi_{]-0.25,0.25[\times]-2.35,-1.65[} \end{bmatrix}(\mathbf{x}),$$

$$\begin{aligned} &\boldsymbol{\gamma}^1(\mathbf{x}) = (1,0), \quad \varepsilon_1 = 0.8, \quad \alpha_1 = \pi/4, \\ &\boldsymbol{\gamma}^2(\mathbf{x}) = (0,1), \quad \varepsilon_2 = 0.9, \quad \alpha_2 = \pi/4. \end{aligned} \qquad l = 0.2\,.$$

In order to include the presence of the obstacle in the computational domain, we put $R_{\omega_1} = 2$ in the evaluation of the nonlocal terms.

The numerical solutions computed with FD-MS-WENO3 with 240×240 points ($h = 1/40$) at three different simulation times $T = 0.6$, $T = 1.2$ and $T = 3.4$ are displayed in Figure 5 without the obstacle and in Figure 6 with the obstacle located at the optimal position given by the solution of the optimization problem (15), which is $\mathbf{x}_0 = (-0.07964469, 0.25297659)$. The obstacle is obtained using $10 \times 2 \times |\mathcal{I}_{\text{opt}}| = 20$ iterations, with an optimal cost value $T_{\text{opt}} = 1.244$, and at computational time $\mathcal{T}_{\text{comp}} = 12851.15\,[s]$ respectively.

As in [9], we notice that the speed of both populations is influenced by their own density and the presence of obstacles, and they deviate from their preferred trajectory when these enter their field of view. Also, we observed that the presence of the obstacle accelerates a lot the evacuation of both populations, see Figure 7, preventing them from obstructing each other and guiding them towards their respective exits. This can be appreciated in Figures 5 and 6 at time T = 3.4. We also note the formation of the expected diagonal lanes at intersection, as already observed in [9, 12].

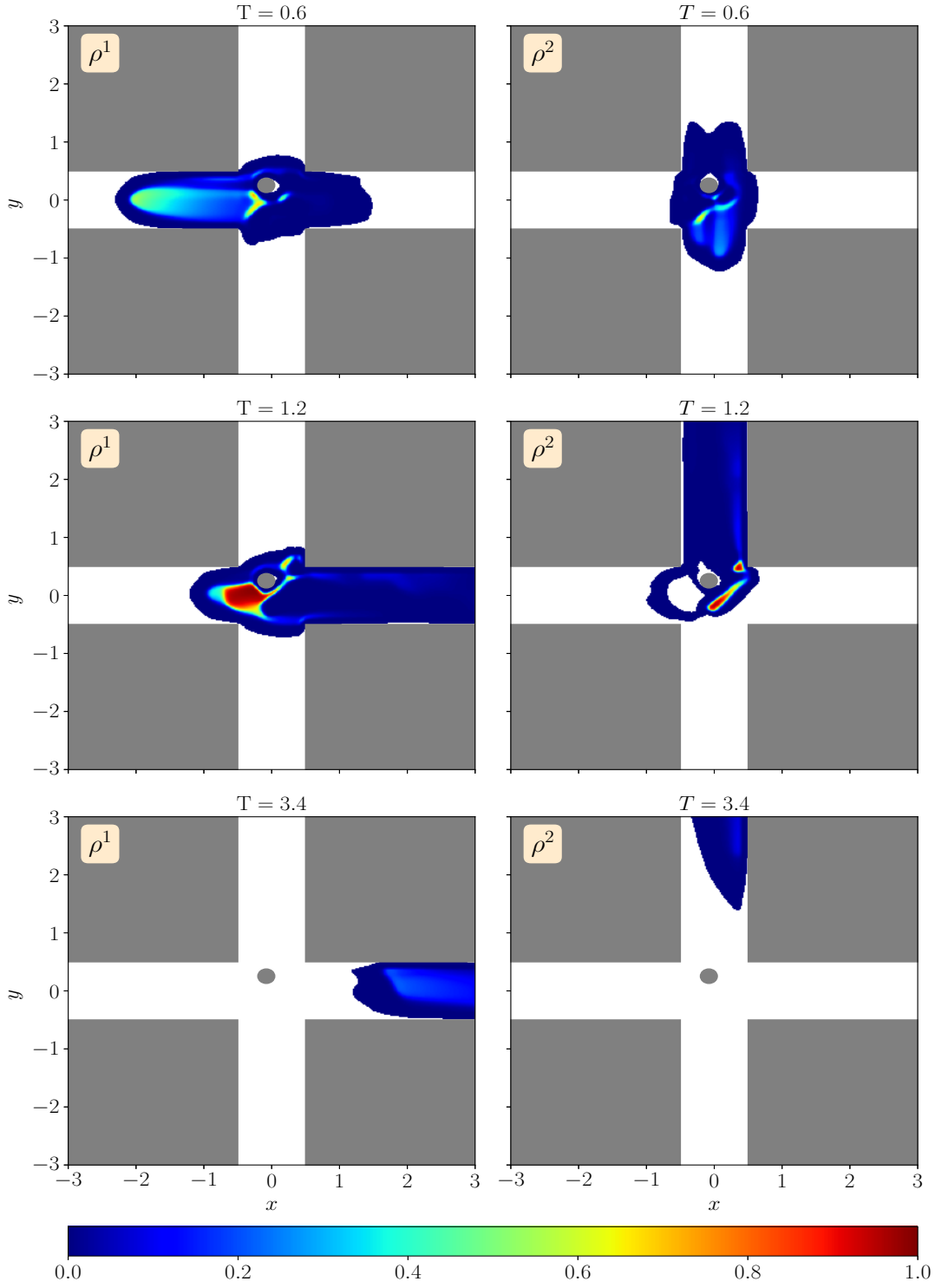

Figure 5: Example 3: Evacuation dynamics, with obstacle, for angle 2α for $\alpha = \pi/4$, at simulated times $T = 0.6$, $T = 1.2$ and $T = 3.4$, for densities ρ^1 (left column) and ρ^2 (right column) respectively.

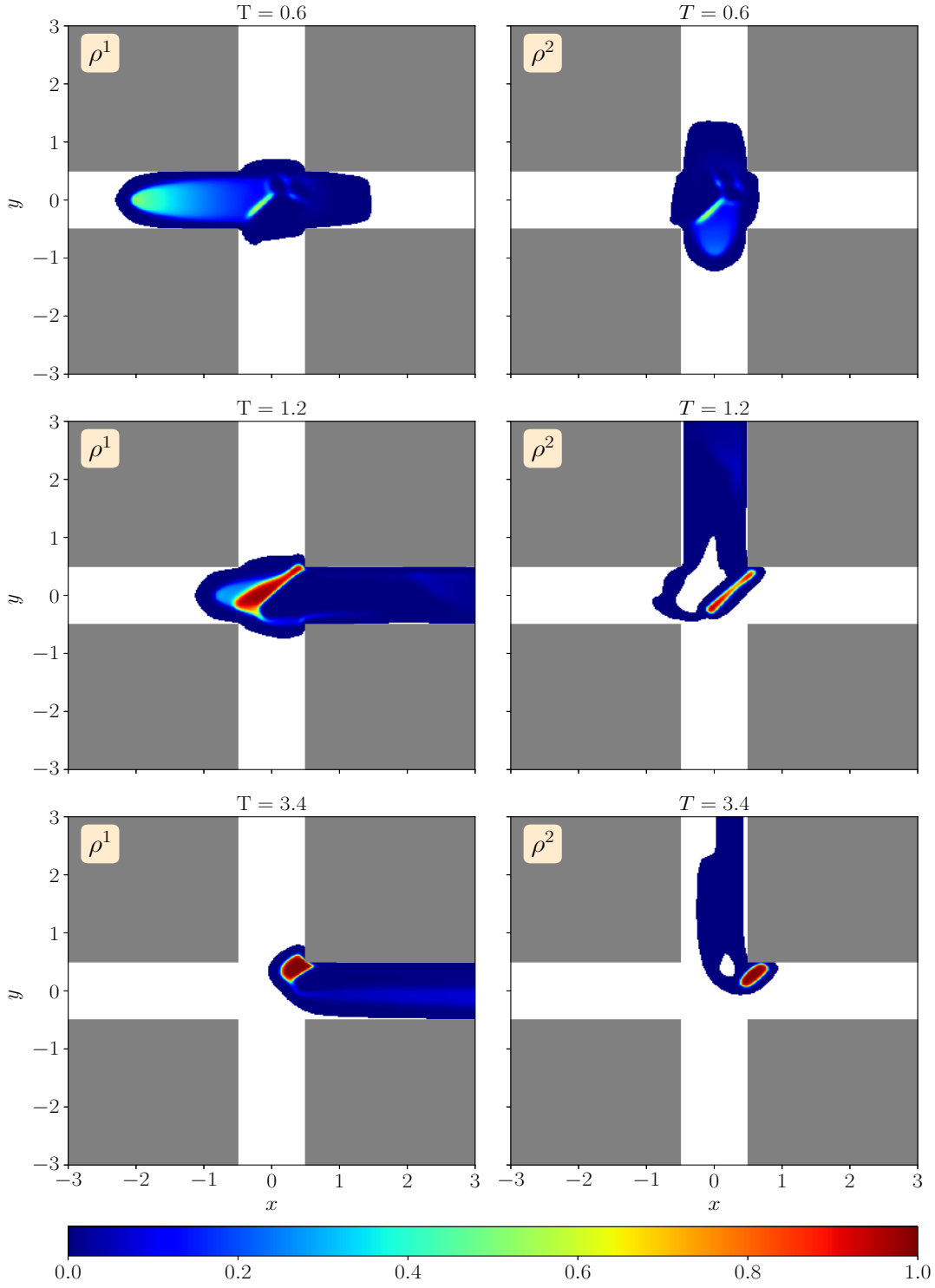

Figure 6: Example 3: Evacuation dynamics, without obstacle, for angle 2α for $\alpha = \pi/4$, at simulated times $T = 0.6$, $T = 1.2$ and $T = 3.4$, for densities ρ^1 (left column) and ρ^2 (right column) respectively.

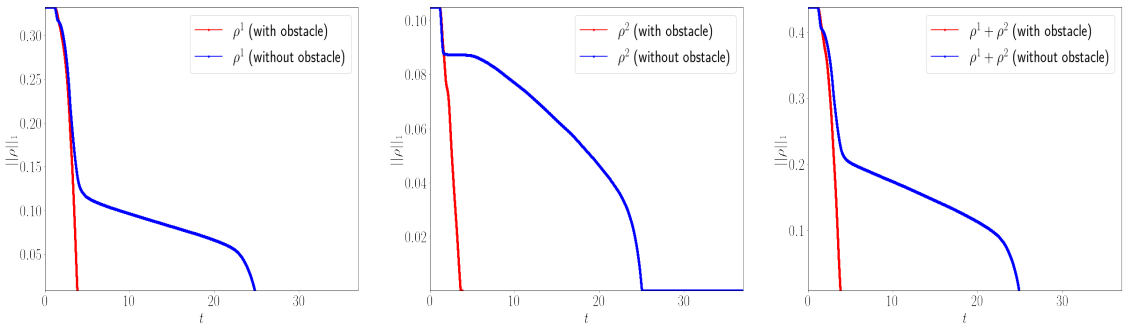

Figure 7: Example 3: Time evolution of the partial masses ρ^1 and ρ^2 and the total mass $\rho^1+\rho^2$ with and without obstacle for angle $\alpha = \pi/4$.

5.4 Example 4: Optimization of obstacle position in a room with one exit

As in Example 3 (Section 5.3), we improve the evacuation speed by using a well placed obstacle, whose optimal position is obtained by solving (15). The pedestrians move from left to right through the space given by

$$\Omega =]0,10[\times]0,5[\setminus\left(\Omega_1^c \cup \Omega_2^c \cup \Omega_3^c\right),$$

where the exit door is located at $\Gamma_1 = \{10\}\times[1.5,3.5]$ and

$$\begin{aligned} &\Omega_{\text{opt}} = \Omega_1^c = \mathbf{B}(\mathbf{x}_0, 0.25), \quad \Omega_{\text{obs}} =]6.5,8.7[\times]1,4[, \quad \mathcal{I}_{\text{opt}} = \{1\},\\ &\Omega_2^c = [9,10]\times[0,1.5], \quad \Omega_3^c = [9,10]\times[3.5,5]. \end{aligned}$$

The vectors fields $\boldsymbol{\mu}^1(\mathbf{x}) = \boldsymbol{\mu}^2(\mathbf{x})$ are computed by solving the Eikonal equation

$$\begin{cases} |\nabla\phi(\mathbf{x})| = 1, & \mathbf{x}\in\hat{\Omega} =]0,10[\times]0,5[\setminus\left(\Omega_2^c\cup\Omega_3^c\right),\\ \phi(\mathbf{x}) = 1 & \mathbf{x}\in\partial\hat{\Omega}\setminus\Gamma_1,\\ \phi(\mathbf{x}) = 0, & \mathbf{x}\in\Gamma_1, \end{cases}$$

and setting $\boldsymbol{\mu}^i(\mathbf{x}) = -\nabla\phi(\mathbf{x})$ for $i=1,2$. The initial condition displayed in Figure 8 and the others parameters are given by

$$\begin{aligned} &\begin{bmatrix}\rho_0^1\\ \rho_0^2\end{bmatrix}(\mathbf{x}) = \begin{bmatrix}0.95\chi_{]1,2.5[\times]0.5,4.5[}\\ 0.6\chi_{]3.5,5.5[\times]0.5,2.5[}\end{bmatrix}(\mathbf{x}), \quad \mathbf{x}\in\Omega,\\ &\boldsymbol{\gamma}^1(\mathbf{x}) = \boldsymbol{\gamma}^2(\mathbf{x}) = (1,0), \quad \alpha_1 = \alpha_2 = \pi/2,\\ &l = 0.4, \quad \varepsilon_1 = 0.8, \quad \varepsilon_2 = 0.9. \end{aligned}$$

In Figures 10 and 11, we display the numerical approximations computed at times $T = 1.9, 7.6$ and 14.4. As in Example 3, we use 20 iterations for the optimizer, obtaining the optimal cost value $T_{\text{opt}} = 53.922$, in a computational time $\text{T}_{\text{comp}} = 168322.99\,[s]$, for the optimal obstacle position $\mathbf{x}_0 = (7.4604323, 1.00036278)$.

We observe that the behaviour between the two groups and with respect to the obstacles is similar at shown in the previous example. On the other hand, the optimal location of obstacle

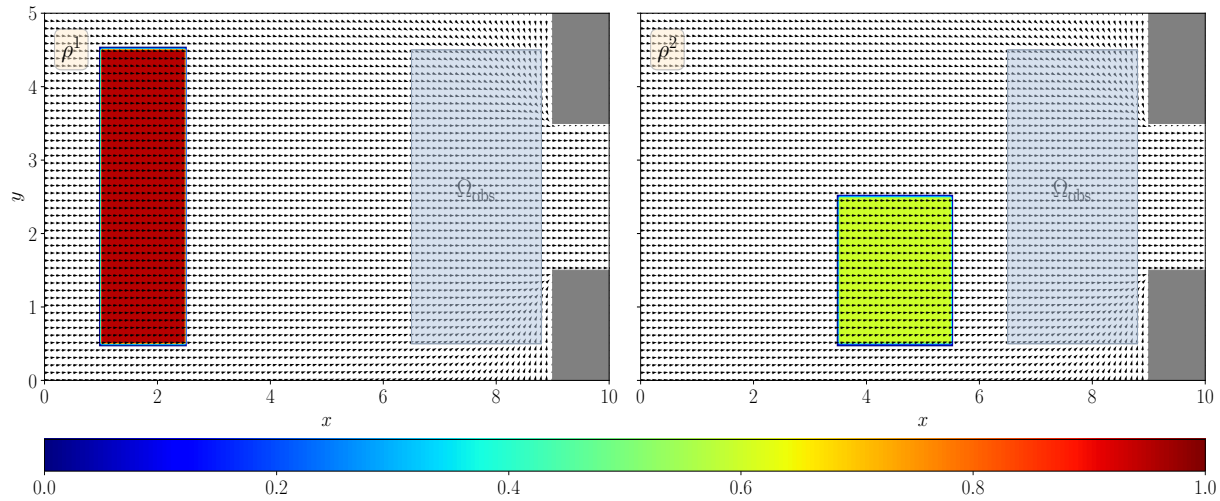

Figure 8: Example 4: Initial conditions ρ^k and vector field $\boldsymbol{\mu}^k$ for each species $k = 1, 2$.

in Figure 10 avoids large density concentrations, allowing for a quicker evacuation of the total population compared to Figure 11. In this case, the impact of the obstacle is less remarkable, see Figure 9.

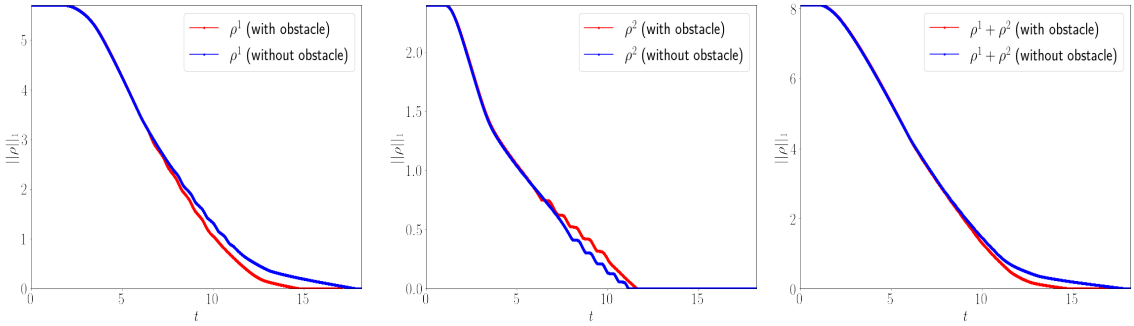

Figure 9: Example 4: Time evolution of the partial masses ρ^1 and ρ^2 and the total mass $\rho^1 + \rho^2$ with and without obstacle for angle $\alpha = \pi/2$..

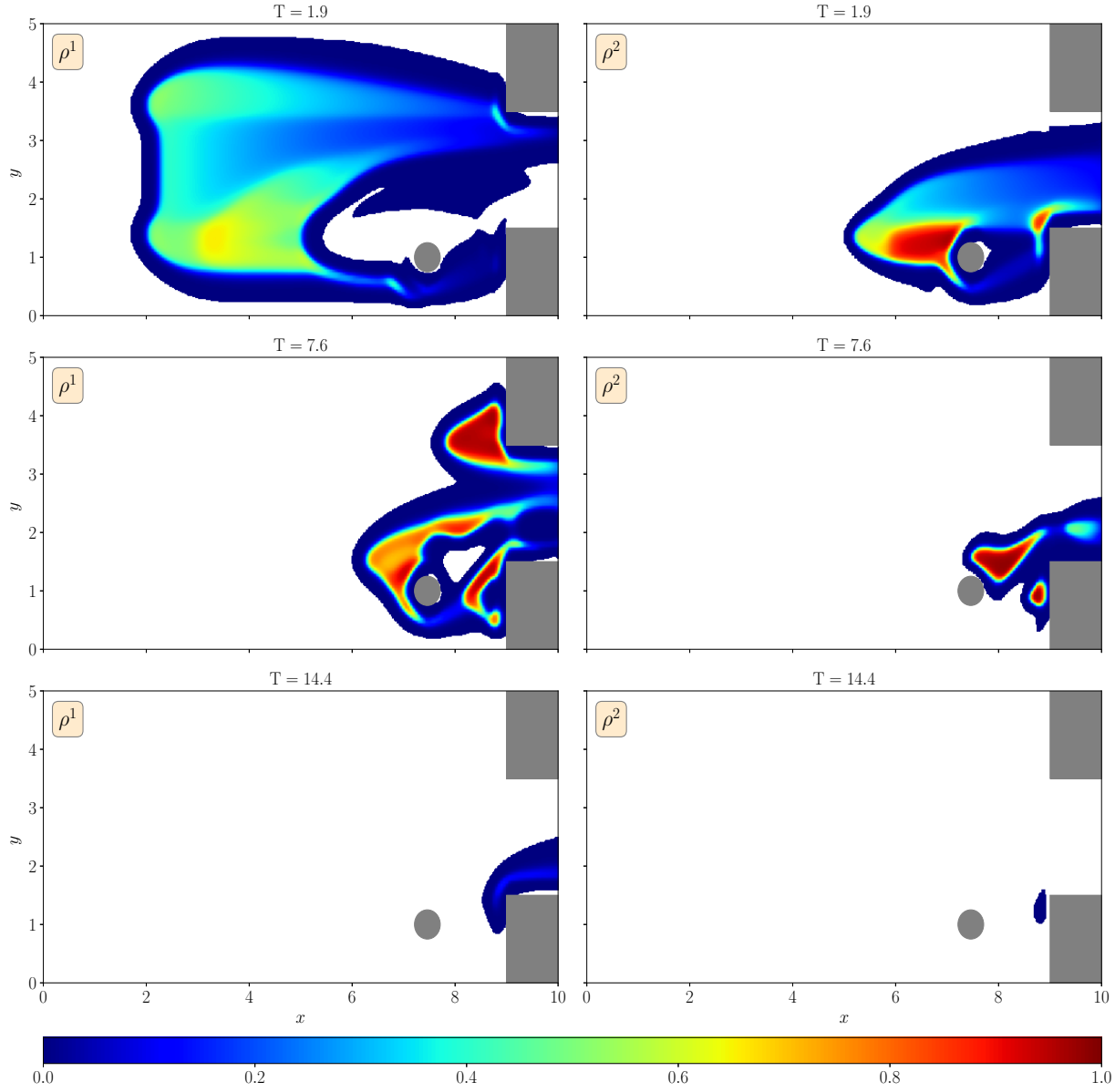

Figure 10: Evacuation dynamics, with obstacle, for angle 2α for $\alpha = \pi/2$, at simulated times $T = 0.6$, $T = 1.2$ and $T = 2.3$, for densities ρ^1 (left column) and ρ^2 (right column) respectively.

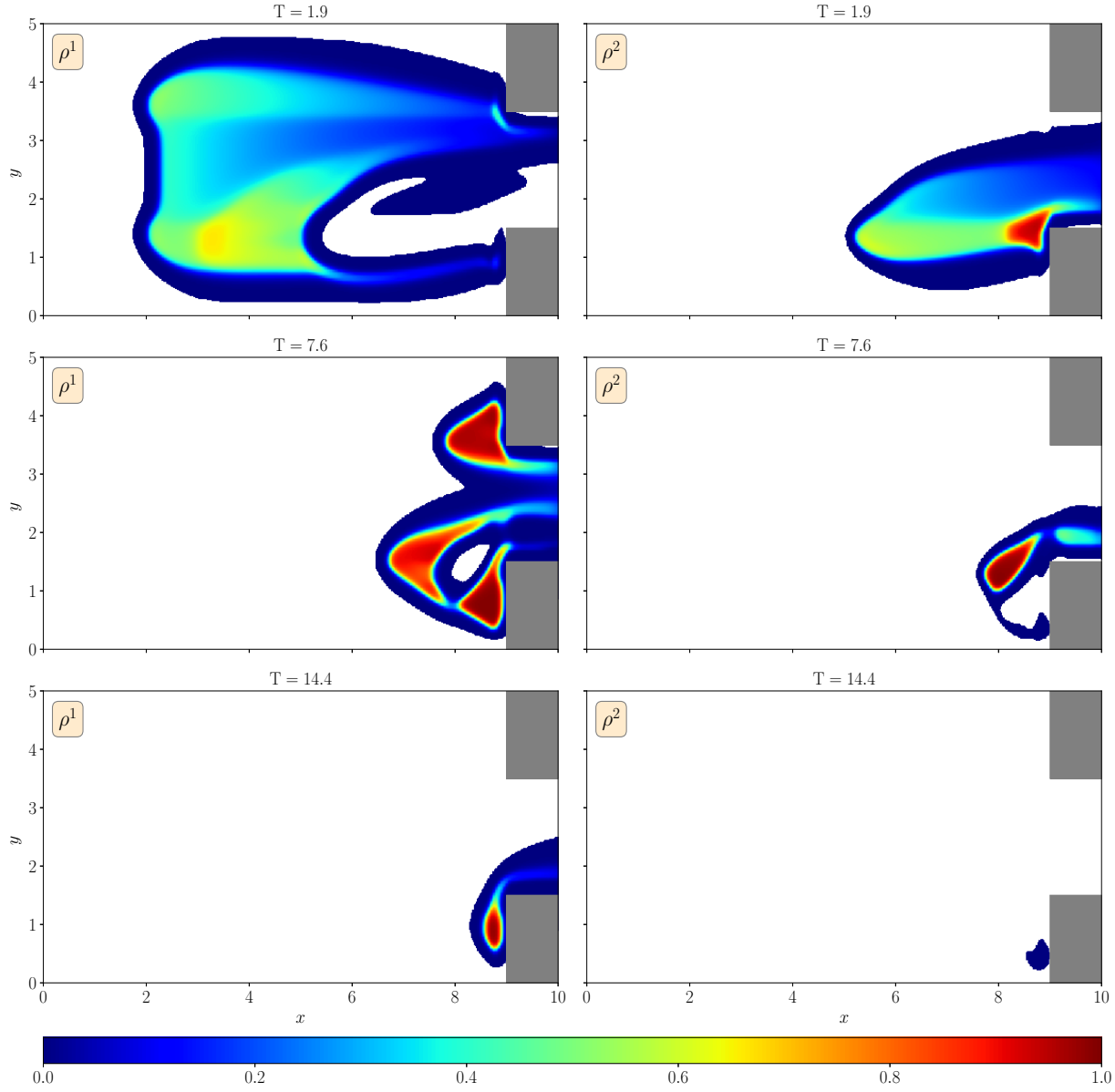

Figure 11: Evacuation dynamics, with obstacle, for angle 2α for $\alpha = \pi/2$, at simulated times $T = 0.6$, $T = 1.2$ and $T = 2.3$, for densities ρ^1 (left column) and ρ^2 (right column) respectively.

Conclusion

In this work we have proposed a nonlocal macroscopic pedestrian flow model for two populations with different destinations trying to avoid each other in a confined environment, where we have considered in the nonlocal terms anisotropic interactions, mimicking the effect of different cones of view, and the presence of walls or other obstacles in the domain, which were incorporated in the density variable. Unlike previous models, we don' t need to be include the presence of obstacles in the computation of the the vector field of preferred directions, thus facilitating the resolution of domain shape optimization problems.

To compute the numerical solution, we proposed a Finite Difference scheme coupled high-order WENO approximations for spatial discretization, a multi-step TVD method for temporal discretization, and a high-order numerical derivative formula to approximate the derivatives of nonlocal terms. The resulting scheme avoid excessive calculations and is faster with respect to numerical schemes proposed in previous works.

Numerical tests corroborate that the proposed model is very sensitive to the changes in the conic vision angles and that each population manages to evade both the obstacles and the other population.

Finally, the evacuation time problem is studied. In particular, the optimal position of the obstacles is obtained through a total travel time minimization processes.

Future work will include simulations of more complex scenarios, the study of the positivity preservation of the proposed high-order scheme and the application of Adaptive Mesh Refinement (AMR) techniques, which concentrate computational effort in regions of strong variation.

Acknowledgements

This work has been supported by: the French government, through the 3IA Côte d'Azur Investments in the Future project managed by the National Research Agency (ANR) with the reference number ANR-19-P3IA-0002; the Inria Associated Team "NOLOCO - Efficient numerical schemes for non-local transport phenomena" (2018-2022); the MATH-Amsud 22-MATH-05 "NOTION - NOn-local conservaTION laws for engineering, biological and epidemiological applications: theoretical and numerical" (2022-2023). LMV was partially supported by ANID-Chile through Centro de Modelamiento Matemático (FB210005).

References

[1] A. Aggarwal, R. M. Colombo, and P. Goatin. Nonlocal systems of conservation laws in several space dimensions. *SIAM J. Numer. Anal.*, 53(2):963–983, 2015.

[2] A. Aggarwal and P. Goatin. Crowd dynamics through non-local conservation laws. *Bull. Braz. Math. Soc. (N.S.)*, 47(1):37–50, 2016.

[3] R. Bürger, P. Goatin, D. Inzunza, and L. M. Villada. A non-local pedestrian flow model accounting for anisotropic interactions and domain boundaries. *Math. Biosci. Eng.*, 17(5):5883–5906, 2020.

[4] R. M. Colombo, M. Garavello, and M. Lécureux-Mercier. A class of nonlocal models for pedestrian traffic. *Math. Models Methods Appl. Sci.*, 22(4):1150023, 34, 2012.

[5] R. M. Colombo and E. Rossi. Nonlocal conservation laws in bounded domains. *SIAM J. Math. Anal.*, 50(4):4041–4065, 2018.

[6] R. M. Colombo and E. Rossi. Modelling crowd movements in domains with boundaries. *IMA J. Appl. Math.*, 84(5):833–853, 2019.

[7] C. De Filippis and P. Goatin. The initial-boundary value problem for general non-local scalar conservation laws in one space dimension. *Nonlinear Anal.*, 161:131–156, 2017.

[8] G. Frank and C. Dorso. Room evacuation in the presence of an obstacle. *Physica A: Statistical Mechanics and its Applications*, 390(11):2135–2145, 2011.

[9] P. Goatin, D. Inzunza, and L. M. Villada. Numerical comparison of nonlocal macroscopic models of multi-population pedestrian flows with anisotropic kernel. *hal-03964740*, 2023.

[10] S. Gottlieb, C.-W. Shu, and E. Tadmor. Strong stability-preserving high-order time discretization methods. *SIAM review*, 43(1):89–112, 2001.

[11] D. Helbing, I. J. Farkas, and T. Vicsek. *Crowd Disasters and Simulation of Panic Situations*, pages 330–350. Springer Berlin Heidelberg, Berlin, Heidelberg, 2002.

[12] S. P. Hoogendoorn, F. L. van Wageningen-Kessels, W. Daamen, and D. C. Duives. Continuum modelling of pedestrian flows: From microscopic principles to self-organised macroscopic phenomena. *Physica A: Statistical Mechanics and its Applications*, 416:684–694, 2014.

[13] R. L. Hughes. The flow of human crowds. In *Annual review of fluid mechanics, Vol. 35*, volume 35 of *Annu. Rev. Fluid Mech.*, pages 169–182. Annual Reviews, Palo Alto, CA, 2003.

[14] G. S. Jiang and C. W. Shu. Efficient implementation of weighted ENO schemes. *J. Comput. Phys.*, 126(1):202–228, 1996.

[15] M. Mimault. *Crowd motion modeling by conservation laws.* Theses, Université Nice Sophia Antipolis, Dec. 2015.

[16] C.-W. Shu. High order weighted essentially nonoscillatory schemes for convection dominated problems. *SIAM Review*, 51(1):82–126, 2009.

[17] M. Twarogowska, P. Goatin, and R. Duvigneau. Macroscopic modeling and simulations of room evacuation. *Appl. Math. Model.*, 38(24):5781–5795, 2014.

[18] J. Von Zur Gathen and J. Gerhard. *Modern Computer Algebra.* Cambridge University Press, 2013.